International Journal of Pharmaceutics: X 4 (2022) 100134

Contents lists available at ScienceDirect

International Journal of Pharmaceutics: X

journal homepage: www.sciencedirect.com/journal/international-journal-of-pharmaceutics-x

Tailored hyaluronic acid-based nanogels as theranostic boron delivery systems for boron neutron cancer therapy

Simon Coninx [a], Ghadir Kalot [b], Amélie Godard [c], Ewen Bodio [c], Christine Goze [c], Lucie Sancey [b], Rachel Auzély-Velty [a,*]

[a] Université Grenoble Alpes, Centre de Recherches sur les Macromolécules Végétales (CERMAV)-CNRS, Grenoble, France
[b] Université Grenoble Alpes, Institute for Advanced Biosciences, INSERM U 1209, CNRS UMR 5309, 38000 Grenoble, France
[c] Institut de Chimie Moléculaire de l'Université de Bourgogne, Université de Bourgogne-Franche-Comté, CNRS UMR, 6302 Dijon, France

ARTICLE INFO

Keywords:
Nanogel
Hyaluronic acid
Boron neutron capture therapy
Aza-BODIPY
Theranostic
Boron compound
^{10}B-BSH

ABSTRACT

Boron-rich nanocarriers possess great potential for advanced boron neutron capture therapy (BNCT) as an effective radiation treatment for invasive malignant tumors. If additionally, they can be imaged in a non-invasive and real-time manner allowing the assessment of local boron concentration, they could serve for dose calculation and image-guided BNCT to enhance tumor treatment efficacy. To meet this challenge, this study describes the design of a theranostic nanogel, enriched in ^{10}B and fluorescent dye, to achieve selective imaging, and sufficient accumulation of boron at the tumor site. The boron-rich and fluorescent nanogels can be easily obtained via temperature triggered-assembly of hyaluronic acid (HA) modified with a thermoresponsive terpolymer. The latter was specifically designed to enable the efficient encapsulation of the fluorescent dye – an aza-boron-dipyrromethene (aza-BODIPY) – linked to ^{10}B-enriched sodium borocaptate (BSH), in addition to induce nanogel formation below room temperature, and to enable their core-crosslinking by hydrazone bond formation. The HA nanogel considerably concentrates aza-BODIPY-BSH into the hydrophobic nanodomains made of the terpolymer chains. Here, we present the detailed synthesis of the HA-terpolymer conjugate, nanogel formation, and characterization in terms of size, morphology, and stability upon storage, as well as the biological behavior of the boron nanocarrier using real-time fluorescence imaging in cells and in vivo. This work suggested the potential of the theranostic HA nanogel as a boron delivery system for the implementation of BNCT in brain cancer and sarcoma.

1. Introduction

Boron neutron capture therapy (BNCT) is a targeted therapy based on the property of the isotope ^{10}B (~ 20% of B isotopes) to capture thermal neutrons, decaying into two highly energetic α particles (^{4}He) and ^{7}Li nuclei by the ^{10}B(n,a)^{7}Li fission reaction. Both particles are very efficient to destroy cells in a short range in the tissue (5–10 μm), due to their high linear energy transfer (LET) properties. Therefore, a strong and specific accumulation of ^{10}B into cancer tissue (~ 20–50 μg ^{10}B/g tissue) can allow the local destruction of tumor cells while sparing the surrounding healthy tissues. Currently, two molecules are used in clinical trials for this purpose and are most of the time co-administered: namely BPA (^{10}B-*p*-boronophenylalanine, $C_9H_{12}^{10}BNO_4$) and BSH (sodium mercaptoundecahydro-closo-dodecaborate, $Na_2^{10}B_{12}H_{11}SH$). BPA accumulates preferentially in the tumor with a Tumor/Surrounding tissue ratio > 2.5 (minimum ratio that should be reached for BNCT application), but the molecule contains only one boron atom (Skwierawska et al., 2022). BSH clusters 12 boron atoms, but possesses a less favorable tumor accumulation (Malouff et al., 2021; Sauerwein et al., 2012).

Therefore, in order to improve the boron content in tumors, several strategies are developed, including the use of small molecules with targeting properties such as the modified boron-derived tyrosine, fluoroboronotyrosine FBY (Li et al., 2019), BSH coupled or linked to cell penetrating peptides (Michiue et al., 2014; Nakase et al., 2019), or larger boron carriers as nanoparticles (Feiner et al., 2021; Kikuchi et al., 2016; Shi et al., 2018). The use of nanoparticles increases the circulation time of the boron agents, and facilitates specific tumor accumulation and theranostic applications. Several types of nanoparticles (NPs) such as liposomes (Li et al., 2022; Shirakawa et al., 2021), dendrimers

* Corresponding author.
E-mail address: rachel.auzely@cermav.cnrs.fr (R. Auzély-Velty).

https://doi.org/10.1016/j.ijpx.2022.100134
Received 10 October 2022; Accepted 11 October 2022
Available online 14 October 2022

(Gonzalez-Campo et al., 2013), and block copolymer NPs (Huang et al., 2021; Nomoto et al., 2021; Ruan et al., 2016; Sumitani and Nagasaki, 2012; Yoneoka et al., 2018) have been evaluated as potential delivery systems. In these examples, boron compounds were either encapsulated in or covalently linked to nanoparticles supposed to accumulate in tumor area via the enhanced permeability and retention (EPR) effect (Pulagam et al., 2019; Sumitani et al., 2012). While the macromolecular approaches may improve specific boron delivery for BNCT,(Pitto-Barry, 2021) they still have limitations such as low boron content per unit weight, and/or complicated and time-consuming particle synthesis.

In addition, the dose calculation is necessary for an optimized precision medicine and the development of adequate treatment planning programs. The amount of ^{10}B accumulated in the tissue directly affects the local production of alpha particles and Li nuclei that induces the cell killing effect. Currently, boron is quantified from blood sampling, and the amount accumulated in the tissue is estimated from previous experimentations, but this method is not accurate nor personalized. Therefore, present developments are focused on theranostic compounds able to track and to quantify in real time the compounds in the patient using nuclear imaging or magnetic resonance imaging (Ho et al., 2022; Kono et al., 2017), to determine the ^{10}B concentration within the different tumor lesions and the surrounding tissues (Dymova et al., 2020).

In this perspective, our strategy consists in the development, through a fast route, of theranostic nanogels, enriched in ^{10}B and fluorescent dye for preclinical evaluation, that are biocompatible and biodegradable.

Hyaluronic acid (HA), a polysaccharide which is a main component of the extracellular matrix, was selected as hydrophilic component due its biocompatibility, biodegradability and the existence of various functional groups that are accessible for chemical modification (Choi et al., 2012). As HA can be recognized by cell surface CD44 receptors that are overexpressed by several cancer cells,(Auzenne et al., 2007; Draffin et al., 2004; Luo and Prestwich, 1999; Qhattal and Liu, 2011) this polysaccharide has been previously investigated as a potential carrier for the targeted delivery of boron to cancer cells to maximize the effectiveness of BNCT (Di Meo et al., 2007; Zaboronok et al., 2015). Yet, there was no evidence for effective in vivo targeting.(Di Meo et al., 2007) Herein, the nanogels are prepared by temperature-induced self-assembly of HA (Rippe et al., 2019a), suitably modified with a custom-made thermoresponsive terpolymer (Fig. 1). Spontaneous nanogel formation is due to the dehydration of the grafted terpolymer chains when heated above the cloud point temperature. Here, the key to our strategy is the efficient entrapment of an aza-BODIPY-BSH conjugate, resulting from the coupling of ^{10}B-enriched BSH to a near-infrared (NIR)-emitting aza-boron-dipyrromethene derivative (Kalot et al., 2020) (Fig. 1), thereby creating a theranostic system. For fluorescence imaging, aza-BODIPYs were selected to preferentially work in the NIR-II optical region, as compared to the visible/NIR-I optical region of the BODIPY compounds (Bertrand et al., 2018).

The terpolymer, composed of diacetone acrylamide (DAAM), *N,N*-dimethylacrylamide (DMA) and *n*-butyl acrylate (BA), was specifically designed to enable efficient encapsulation of the poorly water-soluble aza-BODIPY-BSH (at least 40 μg ^{10}B/mL) in the nanogels, in addition to allow their formation by temperature-triggered self-assembly and their core-crosslinking by hydrazone bond formation (Fig. 1). We further assessed the biological behavior of these new theranostic nanogels with real-time fluorescence imaging in cells and in vivo.

2. Material and methods

2.1. Materials

Hyaluronic acid (Mw = 40 kg/mol) was purchased from Lifecore (USA). Diacetone acrylamide, *N,N*-dimethylacrylamide, *n*-butyl acrylate, 2,2-azobis(2-methylpropionitrile) (AIBN), 4-cyano-4-[(dodecylsulfanylthiocarbonyl)sulfanyl]pentanoic acid (CDSPA), *n*-butylamine, ethanolamine, trioxane, aluminum oxide, phosphate buffer saline (PBS, pH 7.4), Tris-(2-carboxyethyl) phosphine hydrochloride (TCEP), mercaptopropionic acid (MPA), 4-(4,6-dimethoxy-1,3,5-triazin-2-yl)-4-methylmorpholinium chloride (DMTMM), 1-hydroxybenzotriazole (HOBt), *N,N*-diisopropylcarbodiimide (DIC), sodium tetraborate, carbazole isophtalic acid dihydrazide (IDH) were purchased from Sigma-Aldrich-Fluka (France). Boc-cysteamine and divinylsulfone (DVS) were obtained from Alfa Aesar. Presto Blue®, Dulbecco's Modified Eagle Medium (DMEM), L-glutamine, fetal bovine serum (FBS), non-essential amino acids were provided by Thermo Fisher Scientific. Cyanine 7-

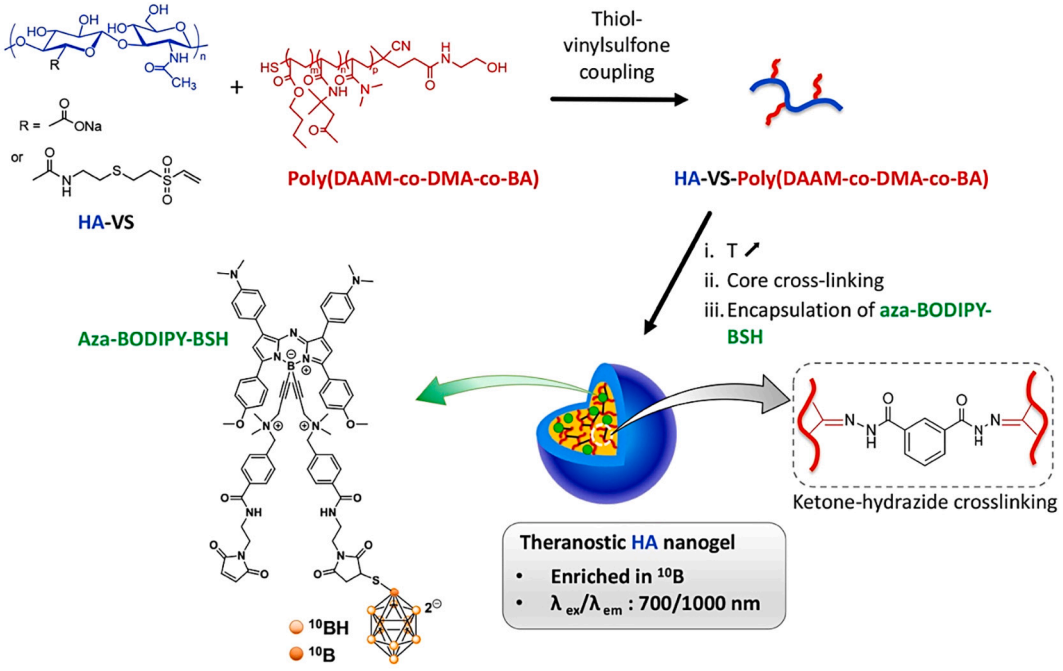

Fig. 1. Formation of theranostic nanogels based on hyaluronic acid on which poly(DAAM-*co*-DMA-co-BA) chains are grafted via thiol-vinylsulfone (VS) coupling. "R" is used to indicate that vinylsulfone groups are randomly grafted along the HA chain via amine bond formation with the carboxylate groups of HA.

amine (Cy7-amine) was purchased from Lumiprobe. All chemicals were used without any further purification. The positively charged resin, diethylaminoethyl cellulose (DEAE) was purchased from GE Healthcare Life Science. The water used in all experiments was purified by an Elga Purelab purification system, with a resistivity of 18.2 MΩ cm. CDSPA was modified with ethanolamine as described in Supporting Information (Fig. S1 and S2). Cysteamine vinyl sulfone (CVS) was synthesized according to a procedure described previously (Stewart et al., 2018) with slight modifications (Supporting Information, Fig. S3). The aza-BODIPY-BSH (^{10}B enrichment of BSH > 99.5%) was synthesized by Dr. A. Godard (Kalot et al., 2020). The fluorescence and absorbance spectra of aza-BODIPY-BSH in DMSO as well as the variation of fluorescence with concentation in serum are shown in Fig. S4 and S5, respectively.

2.2. Characterization methods

2.2.1. Analysis of the polymers by ^{1}H NMR and SEC

^{1}H NMR spectra were recorded at 25 °C using a Bruker AVANCE III HD spectrometer operating at 400 MHz. Deuterium oxide (D_2O), dimethysulfoxide-d_6 (DMSO-d_6) and deuterated chloroform ($CDCl_3$) were obtained from SDS (Vitry, France). All spectra were recorded by applying a 45° tip angle for the excitation pulse, and a 10 s recycle delay. Chemical shifts (δ in ppm) are given relative to external tetramethylsilane (TMS = 0 ppm) and calibration was performed using the signal of the residual protons of the solvent as a secondary reference.

The number-average molar mass (M_n), the weight-average molar mass (M_w) and the dispersity ($Đ$) of poly(DAAM-*co*-DMA-co-BA) were determined by size exclusion chromatography (SEC). Measurements were conducted in DMF with 0.01 M LiCl at 40 °C and a flow rate of 0.6 mL/min using a SEC Agilent Technologies 1260 Infinity Multi Detector Suite (MDS) GPC/SEC System. This SEC apparatus was equipped with a RI detector, a dual angle light scattering detector, a quaternary pump and several columns (Shodex Asahipak GF-1G 7B, GF-7 M HQ, and GF-310 HQ). The absolute molar masses were determined using a dn/dc of 0.105 mL/g.

2.2.2. Determination of the cloud point of poly(DAAM-co-DMA-co-BA)

The cloud point temperature (T_{cp}) of poly(DAAM-co-DMA-co-BA) was determined by turbidity measurements (λ = 500 nm) performed on a Varian Cary 50 Scan. The samples were prepared in PBS (0.5 g/L) at 4 °C. The light transmittance was measured during at least two controlled cooling/heating cycles using a 1 °C interval. The T_{cp} was considered to be the temperature at which the light transmittance was 50% of that obtained for the same sample at low temperature (5 °C or 15 °C depending on the poly(DAAM-co-DMA-co-BA) sample).

2.2.3. Determination of the critical Aggregation Temperature (CAT) of HA-VS- poly(DAAM-co-DMA-co-BA)

The CAT of HA-VS-poly(DAAM-co-DMA-co-BA) in aqueous solution was assessed using a Zetasizer NanoZS Malvern Instruments apparatus equipped with a HeNe laser at 173° and a temperature controller. A solution of HA-VS-poly(DAAM-co-DMA-co-BA) in PBS at a concentration of 0.5 mg/mL was filtered through a 0.8 µm polycarbonate filter and heated from 5 to 45 °C using a 5 °C interval. The CAT was considered to be the temperature at the intersection between the lower horizontal portion of the plotted curve (average scattered intensity versus temperature dependence) and the tangent line of the curve. The size and size distribution of nanogels were simultaneously measured with the CAT by dynamic light scattering (DLS) using a Zetasizer NanoZS Malvern Instruments apparatus operating with a HeNe laser at 173°.

2.2.4. Analysis of the nanogels by Dynamic Light Scattering (DLS) and transmission electron microscopy (TEM)

The size distribution and mean nanogels size were studied by DLS, using the equipment described in the previous section. The hydrodynamic diameters were calculated from diffusion coefficients using the Stokes-Einstein equation. All correlogram analyses were performed with the software supplied by the manufacturer. All the measurements were performed in PBS (pH 7.4).

For TEM analysis, a droplet of nanogels suspension (0.5 g/L in PBS) was deposited on a plasma-treated carbon-coated grid, negatively stained with 2% (*w/v*) UranyLess (Delta Microscopies) and observed at 200 kV using a JEOL 2100 microscope equipped with a RIO16 camera (GATAN).

2.2.5. Determination of the entrapment efficiency (EE) and drug loading (DL)

A reversed-phase (RP)-HPLC method was used to determine the amount of aza-BODIPY-BSH encapsulated in the nanogels. The HPLC system consisted of a Prominence HPLC system (Shimadzu, Kyoto, Japan), containing a vacuum degasser, a double micro-volume piston pump, an auto-sampler, a thermostatic column compartment and an ultraviolet detector (model SPD-20A (Tokyo, Japan)). The UV detector was set at a wavelength of 650 nm, and the detector was linked to LabSolutions Software (Shimadzu Corporation, Tokyo, Japan). Reversed-phase chromatography was performed on a C18 column (150 × 3.0 mm, particle size 5 µm; Shimadzu, Kyoto, Japan). The mobile phase used was 0.1% trifluoroacetic acid (TFA) in water and 0.1% TFA in acetonitrile (1:1 *v*/v). The injection volume was 15 µL, with a flow rate of 1 mL/min and column temperature of 25 °C. The retention time of aza-BODIPY-BSH was 5.3 min. The quantification method was specific and linear (y = 4531× + 11,991, r = 0.9946), using five concentrations in the range of 0.1– 100 µg/mL of aza-BODIPY-BSH.

The entrapment efficiency was determined by HPLC quantification of the amount of aza-BODIPY-BSH loaded in the nanogels. After freeze-drying of the samples, aza-BODIPY-BSH was recovered by solubilization in acetonitrile upon stirring for 3 h, with 5 min sonication steps after each 1 h interval. After centrifugation (10,000 rpm for 30 min), to remove the HA derivative and buffer salt, and filtration through a 0.45 µm membrane filter, the amount of aza-BODIPY-BSH was determined by RP-HPLC. Encapsulation efficiency was calculated as EE (%) = (recovered aza-BODIPY-BSH mass/ feed aza-BODIPY-BSH mass) × 100, and drug loading as DL (%) = [recovered aza-BODIPY-BSH mass / (recovered aza-BODIPY-BSH mass + nanogel mass)] × 100.

2.3. Syntheses

2.3.1. Syntheses of poly(DAAM-co-DMA-co-BA)

DMA, DAAM and BA were passed through a column of basic alumina prior to polymerization. Then, the three monomers, CDSPA modified with ethanolamine, AIBN and trioxane were mixed together in 7 mL anhydrous dioxane using different feed ratios (see Table 1). The mixture was purged with nitrogen at room temperature for 30 min and then, immersed in a thermostated oil bath at 75 °C. Samples were removed periodically by syringe to assess the monomer conversions by ^{1}H NMR spectroscopy (Fig. S6). The polymerization was quenched, after a predetermined time, by removing the polymerization from heat and exposing the reaction solution to air. The resulting poly(DAAM-*co*-DMA-co-BA) was isolated by precipitation (×3) in cold hexane, dried under vacuum and analyzed by ^{1}H NMR spectroscopy (Fig. S7 and S8).

Table 1
Conditions for the synthesis of the different Poly(DAAM-*co*-DMA-co-BA) samples by the RAFT method.

Poly (DAAM-co-DMA-co-BA)	CTA (mmol)	DAAM (mmol)	DMA (mmol)	BA (mmol)	AIBN (mmol)	Trioxane (mmol)
1	0.0982	5.91	4.73	1.18	0.0138	0.33
2	0.0976	5.91	5.02	0.887	0.0146	0.33
3	0.0971	5.91	5.32	0.591	0.0146	0.33
4	0.0966	5.91	5.61	0.296	0.0144	0.33

Samples taken before and during the polymerization were analyzed by ^{1}H NMR to determine monomers conversion (Fig. 2, S9, S10 and S11. The M_n, M_w and $Đ$ values of the copolymer were determined by SEC in DMF.

2.3.2. Synthesis of HA-VS-poly(DAAM-co-DMA-co-BA)

The poly(DAAM-co-DMA-co-BA) terpolymer **1** was subjected to aminolysis to convert the RAFT (Reversible Addition Fragmentation chain Transfer) end-group to a thiol. Briefly, the copolymer (600 mg, 0.044 mmol) was solubilized in CH_2Cl_2 (8.8 mL) and *n*-butylamine (6.5 mL, 0.065 mol) was added. After 5 min under stirring, the reaction mixture was concentrated under reduced pressure, resulting in syrup that was solubilized in CH_2Cl_2 (5 mL). The terpolymer was recovered by precipitation (2 ×) in cyclohexane (200 mL) and dried under vacuum at 40 °C to obtain a white powder. Next, the thiol-capped terpolymer (500 mg, 0.0370 mmol) was solubilized in 8 mL of water and TCEP (10.6 mg, 0.0370 mmol) was added. After 1 h 30 min of stirring at 4 °C under nitrogen atmosphere, the terpolymer was purified by dialysis against deionized water for 5 h under N_2 at 4 °C and the solution was added to a solution of HA functionalized with vinylsulfone (HA-VS, 40 mg, 0.0962 mmol) in water to perform the thiol-vinylsulfone coupling reaction.

To prepare the HA-VS derivative, HA (50 mg, 0.125 mmol) was dissolved in 25 mL of a H_2O/DMF (3:2 v/v). Next, vinylsulfone-cysteamine (3.86 mg, 0.0125 mmol) and DMTMM (34.6 mg, 0.125 mmol) were added. The pH was adjusted to 6.5 by addition of 0.1 M HCl and the reaction mixture was stirred for 18 h at room temperature. The resulting product was purified by diafiltration using a membrane Amicon Ultracel MWCO 10 KDa and recovered in pure water. Then, one part of the solution of HA-VS (0.028 mmol) was taken to determine the degree of substitution (DS, average number of substituting group per repeating disaccharide unit) of HA-VS by ^{1}H NMR spectroscopy after freeze-drying (Fig. S10). This was found to be equal to 0.09.

The HA-VS (40 mg, 0.0962 mmol) was reacted with the terpolymer **1** (500 mg, 0.0370 mmol) in water (20 mL) at pH 9 for 6 h under N_2 at 4 °C. The remaining VS groups were then converted to carboxylic acid groups by addition of MPA (1 µL). To this end, the pH of the reaction medium was adjusted to 8 and the reaction medium was further stirred for 2 h under N_2 at 4 °C. The reaction medium was then transferred to an ion exchange column using DEAE Sepharose CL-6B as a weak-anion exchanger and stored overnight at 4 °C. The non-reacted terpolymer was eluted at 4 °C with deionized water. The HA-VS-poly(DAAM-co-DMA-co-BA) bound to the resin was then eluted with 1 M NaCl (80 mL) at 4 °C. The solution of the HA conjugate was then purified by dialysis (MWCO 6–8 kDa) against deionized water and freeze-dried to recover HA-VS-poly(DAAM-co-DMA-co-BA) as a white powder.

2.3.3. Labelling of HA-VS-poly(DAAM-co-DMA-co-BA) with sulfo-cyanine7

Fluorescent HA-VS-poly(DAAM-co-DMA-co-BA) was prepared by grafting the dye Cy7-amine on terpolymer **1** by an amine-acid coupling reaction using DMTMM as a coupling agent (Rippe et al., 2019b). To this end, HA-VS-poly($DAAM_{44}$-*co*-DMA_{43}-co-BA_9) (10 mg, 0.0093 mmol) was solubilized in water/DMF (1:1 *v*/v; 6 mL) and DMTMM (2.57 mg, 0.0093 mmol) was added to the solution, followed by adjusting the pH to 6.5. After 30 min of stirring, Cy7-amine (0.375 mg, 0.0005 mmol) solubilized in water/DMF (1:1 *v*/v) at a concentration of 5 g/L was added to the reaction mixture. After stirring at room temperature for 24 h, the product was purified by dialysis using a membrane MWCO 6–8 kDa against a mixture of water/ethanol (2:1 v/v) then, against deionized water for 48 h and finally, was recovered by freeze-drying. The DS in Cy7 determined by UV–vis spectroscopy ($\lambda = 680$ nm) was found to be 0.02.

2.3.4. Synthesis of cross-linked nanogels and encapsulation of aza-BODIPY-BSH

To a solution of HA-VS-poly(DAAM-co-DMA-co-BA) (10 mg, 0.0093 mmol) with a DS of 0.08 at a concentration of 0.5 g/L in PBS (pH 5) at 40 °C, isophtalic acid (6.4 mg, 0.032 mmol) solubilized in DMSO (10 g/L) was added under stirring. After stirring at 40 °C for 18 h, the nanogels suspension was transferred into a dialysis bag (MWCO 6–8 kDa) and dialyzed against deionized water for 48 h at 4 °C. The core cross-linked nanogels, labelled with Cy7 or non-labelled, were recovered by freeze-drying.

For the encapsulation of aza-BODIPY-BSH, the fluorochrome was solubilized in DMSO at 20 g/L. Next, different volumes of the fluorochrome solution were added to 1 mL of nanogels solutions (0.5, 1 or 3 g/L in PBS) at 37 °C, and stirred for 2 h. Then, the solutions were filtered through a 0.8 µm polycarbonate filter to remove non-encapsulated molecules. Indeed, in spite of the existence of several charges on aza-BODIPY-BSH, this compound is poorly water-soluble as explained in Supporting Information (Fig. S5).

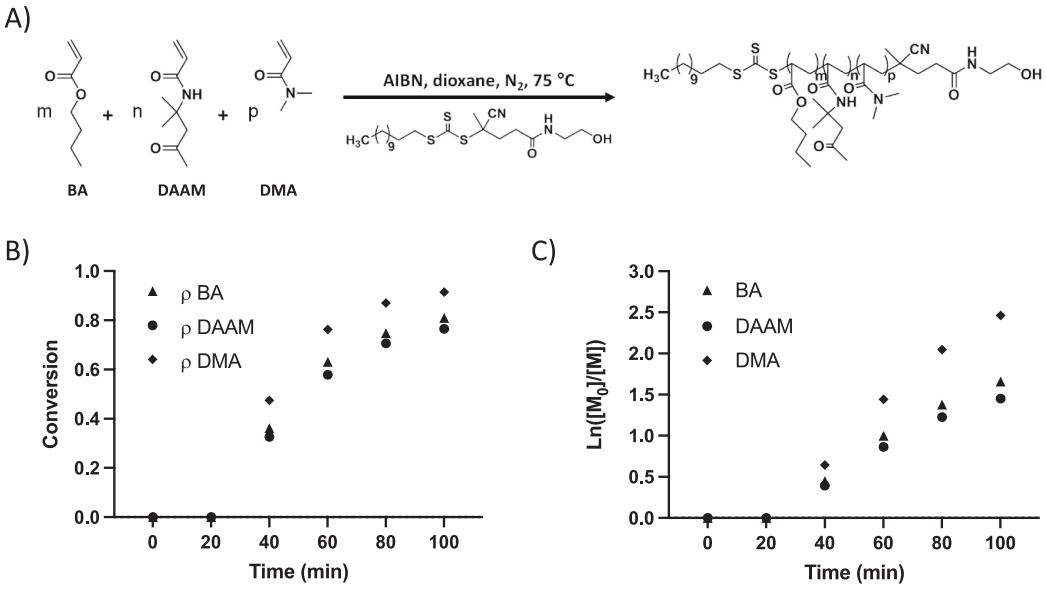

Fig. 2. Synthesis of poly(DAAM-*co*-DMA-co-BA) by the RAFT method. A) Reaction scheme. B) Monomer conversion determined by ^{1}H NMR vs time. C) Pseudo-first-order rate plot.

2.3.5. Lyophilization of nanogels

The crosslinked nanogels in ultrapure water were quickly frozen in liquid nitrogen. After that, they were freeze-dried and stored at −18 °C for 10 weeks. Then, the nanogels were reconstituted with PBS, filtered through a 0.8 μm polycarbonate filter and further evaluated with size and PDI by DLS.

2.4. In vitro experiments

2.4.1. Cell culture

Human endothelial HDMEC cells and glioblastoma U87-MG cells were obtained from ECACC collection. HDMEC were cultured in endothelial cell growth medium (#C-22110, Sigma-Aldrich, St Quentin-Fallavier, France), and U87-MG were cultured in DMEM enriched with 2 mM Glutamine, 1% non-essential amino acids (NEAA), and 10% Fetal Bovine Serum (FBS). Cells were maintained in humidified atmosphere with 5% CO_2, and trypsined for expansion.

2.4.2. Toxicity assay

HDMEC were cultured in 96-well plate one day before investigation. Cells were incubated with molecular linear HA-VS-poly(DAAM-*co*-DMA-co-BA) or HA NG for 24 h. Cell viability was evaluated using Presto Blue assay (Thermo-Fisher scientific), a technique that evaluates the cell's metabolic activity, as described by the manufacturer.

2.4.3. Confocal imaging

U87-MG cells were cultured on Lab-Tek® chamber II 1.5 borosilicate coverglass (Merck, Meylan, France) and incubated with nanogels at 50 μg/mL for 22 h, at 37 °C, 5% CO_2. Then, cells were washed and fluorescence microscopy images were acquired using a confocal laser-scanning microscope (LSM 710 Carl Zeiss, Jena, Germany) in live mode, using a plan apochromat 63× in oil objective. Hoechst 33342 was used to counterstain the cell nuclei (1 μM). Fluorescent signal was obtained with a 633 nm excitation laser (6% of laser power), and collected using a LP736 filter, in APD (avalanche photodiode) mode. To evidence Hoechst staining, 405 nm laser excitation was performed at 2%, and the signal was collected from 425 to 475 nm.

Images were processed using ImageJ software. The experiments were performed at the MicroCell (Optical Microscopy-Cell Imaging) platform, IAB Grenoble.

2.5. Preclinical models and fluorescence imaging

All animal experiments were performed in accordance with the Institutional Animal Care and Use Committee at Grenoble Alpes University. These experiments were also approved by the Animal Ethics Committee of the French Ministry, under the agreement number APAFIS #8782. The experiments were performed at the Optimal (Small Animal Imaging Platform, www.imagerie-optimal.fr/) platform, IAB Grenoble.

2.5.1. Mice experiments

U-87 MG cancer cells (5 million cells per 100 μL PBS) were injected subcutaneously on the right flank of female NMRI nude mice (6–8-week-old) (Janvier Labs, Le Genest-Saint Isle, France). After tumor growth (~two weeks), 6 mice were anesthetized (air/isoflurane 4% for induction and 2% thereafter) and injected intravenously in the tail vein with 200 μL of 3 mg/mL HA-VS-poly(DAAM-*co*-DMA-co-BA) loaded with aza-BODIPY-BSH. Whole-body fluorescence images were acquired before and 2, 24, and 48 h post-administration. At 24 and 48 h post injection, the experiment was ended and the organs were sampled for ex-vivo fluorescence imaging. Acquired images were analyzed using ImageJ software. The fluorescence imaging was performed on a home-made SWIR system (Drs X. Le Guével and V. Josserand) using a Princeton camera 640ST (900–1700 nm) coupled with a laser excitation source at $\lambda = 808$ nm (100 mW/cm^2), and a collection from 1064 to 1700 nm (Le Guevel et al., 2018; Musnier et al., 2019).

2.5.2. In ovo experiments

According to the European regulations, no ethical approval is needed for the scientific experimentations using oviparous embryos. This model was developed to restrict the use of animals and to facilitate upcoming BNCT experiments, according to the described procedure (Kalot et al., 2020). Briefly, fertilized white leghorn chicken eggs (Couvoir de Cerveloup, Vourey, France) were incubated at 38 °C with 55% relative humidity. At day 9, the chorioallantoic membrane (CAM) was gently lacerated and 5×10^6 U87-MG cells mixed with 30 μL of matrigel (Growth Factor Reduced (GFR) Basement Membrane Matrix #354230, Corning® Matrigel® (Wiesbaden, Germany)) were deposited on the lacerated region. At day 12, 50 μL of aza-BODIPY-BSH nanogel formulation were added on top of the grown tumors ($n = 4$ per condition). Images were performed before and 1, 2.5, 5, 24 and 48 h after compound administration using Fluobeam® 800 system (Fluoptics®, Grenoble, France).

3. Results and discussion

3.1. Synthesis of the thermosensitive terpolymer poly(DAAM-co-DMA-co-BA)

The terpolymer was prepared by coupling ethanolamine to CDSPA as a chain transfer agent (Fig. S1 and S2), followed by RAFT polymerization at 75 °C in dioxane under AIBN initiation (Fig. 2A). The molar ratio of monomers: chain transfer agent (CTA) was fixed at 100:0.83 with a DAAM/DMA/BA feed ratio of 1:0.8:0.2. ^{1}H NMR spectroscopy was used to monitor the kinetics of the polymerization (Fig. S6). The kinetic plots proved that, in these reaction conditions, modified CDSPA allowed a good control over the RAFT polymerization of DAAM, DMA and BA resulting in a terpolymer with a final DAAM/DMA/BA composition of 1:0.98:0.21 (Fig. 2B and C).

The resulting terpolymer displayed a low dispersity ($Đ$) value (1.06) with a number average molar mass M_n of 13,300 kg/mol from SEC analysis. Its structural integrity was ascertained using ^{1}H NMR analysis (Fig. S7). The presence of an alcohol function at one end of the terpolymer is due to the modification of the CTA by ethanolamine. Herein, the alcohol group was introduced to obtain a neutral terpolymer and thereby, facilitate the separation of the negatively charged HA-poly (DAAM-co-DMA-co-BA) conjugate from the non-grafted terpolymer by ionic exchange chromatography (see Experimental section). The chemical composition of the terpolymer determined by ^{1}H NMR (Table 2 and Table S1 in Supporting Information) was in good agreement with the value calculated from the conversion and feed ratio of each monomer. Additionally, the M_n value, calculated from the monomer conversions derived from ^{1}H NMR (M_n ~ 13,700 g/mol), correlated well with the molar mass measured by SEC.

The terpolymer exhibited a cloud point temperature of ~10.5 °C, as desired. It should be noted that several RAFT polymerizations were previously conducted by varying the DAAM/DMA/BA feed ratio in order to obtain a T_{cp} around 10 °C (see Table 1, Experimental section). The physico-chemical characteristics of the resulting terpolymers are summarized in Table 2 and their molar mass distributions obtained from SEC are shown in Fig. 3A.

The temperature-responsive properties of the four terpolymers displayed in Fig. 3B shows a broad variation of the T_{cp} by varying the monomer ratios.

3.2. Synthesis and characterization of core-crosslinked nanogels

3.2.1. Coupling of poly(DAAM-co-DMA-co-BA) to HA

Our strategy to couple poly(DAAM-co-DMA-co-BA) **1** to HA relied on a thiol–vinylsulfone coupling reaction taking benefit from the end-terminal thiol of **1** obtained after aminolysis of the terminal trithiocarbonate end group derived from the CTA. For this purpose, HA was first functionalized by amine-acid coupling with cysteamine vinyl sulfone

Table 2
Results from the synthesis of poly(DAAM-*co*-DMA-co-BA) by varying the monomer feed ratios.

Poly(DAAM-*co*-DMA-co-BA)	Final ratio[a,b]	$M_n$exp[b] (g/mol)	M_nSEC[c] (g/mol)	Conversion[a,b] (%)	Nb of monomer units in the terpolymer[b]	$Đ$[c]	Yield (%)
1	1/0.98/0.21	13,300	13,800	76/91/80	44/43/9	1.06	91
2	1/0.95/0.14	11,900	11,500	68/79/68	41/39/6	1.08	88
3	1/1.44/0.15	14,100	14,100	79/93/85	41/60/6	1.10	92
4	1/1.16/0.05	14,500	14,400	72/87/74	49/57/3	1.09	90

[a] DAAM/DMA/BA.
[b] Determined by ^{1}H NMR from the kinetics monitoring of the terpolymerization (see Fig. 2, S9, S10, S11).
[c] Determined by SEC-MALS at 5 g/L in DMF with 0.01 M LiCl.

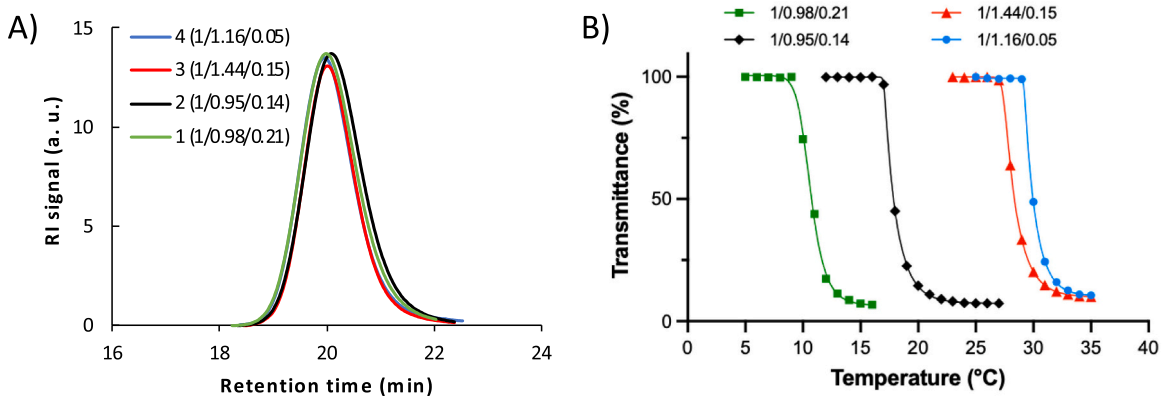

Fig. 3. A) SEC traces of the four poly(DAAM-*co*-DMA-co-BA) samples and B) temperature dependence of the transmittance at 500 nm of aqueous solutions of the terpolymers (0.5 mg/mL in PBS, pH 7.4).

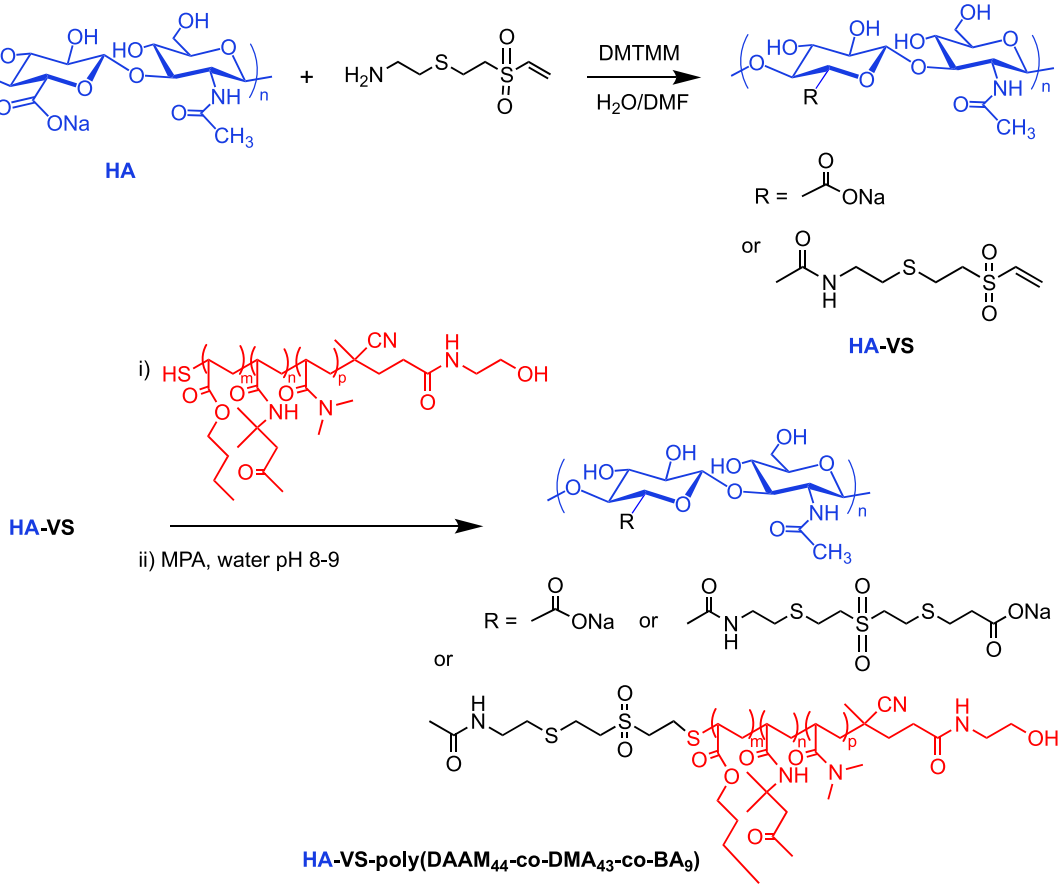

Fig. 4. Synthesis of HA-VS-poly(DAAM-*co*-DMA-co-BA) via thiol-vinylsulfone coupling.

(CVS) that was previously shown to react efficiently with thiol-containing biomolecules in mild aqueous conditions (Grover et al., 2009) (Fig. 4). After purification, the resulting HA-VS derivative, possessing a degree of substitution (DS) of 0.09 from ^{1}H NMR analysis (Fig. S12), was reacted with the terpolymer **1** on which the RAFT end-group was converted to a thiol by aminolysis using *n*-butylamine (Fig. 4). After 12 h reaction, an excess of mercaptopropionic acid (MPA) was added to convert the unreacted VS groups to carboxylic acid ones. The conjugate was subsequently purified via ion exchange chromatography at low temperature (4 °C) to ensure effective removal of the non-grafted terpolymer, followed by a rapid dialysis to remove salt. This purification process, afforded the final product in 87% yield.

Successful grafting of the terpolymer on HA was confirmed by ^{1}H NMR analysis (Fig. 5). In the ^{1}H NMR spectrum, the proton signals at 3 ppm, 2.2 ppm and in the region of 1.8–0.8 ppm arising from poly (DAAM-*co*-DMA-co-BA) can easily be observed. Moreover, the coupling reaction led to complete disappearance of the alkene protons of VS. Digital integration of the signals of the anomeric HA protons and the -CH_3 protons of the BA units of the terpolymer revealed a DS of 0.08. This result indicates that almost all VS groups reacted with the terpolymer.

3.2.2. *Formation of nanogels and their cross-linking via ketone-hydrazide chemistry*

HA-VS-poly(DAAM-co-DMA-co-BA) undergoes temperature-triggered self-assembly into nanogels in phosphate buffer saline (PBS, pH 7.4) owing to the temperature-responsive behavior of the grafted terpolymer. Self-assembly into nanogels is due to the dehydration of the grafted terpolymer chains when heated above a critical temperature, called the critical aggregation temperature (CAT).

The CAT was determined by measuring the light scattering intensity (LSI, expressed in counts per second) of a solution of HA-VS-poly (DAAM-co-DMA-co-BA) in PBS (0.5 g/L) as a function of temperature (Fig. 6A and B). The LSI is followed as it represents the overall quantity of suspended scattering material and depends on particle size (D), concentration (C) and refractive index (LSI ∝ D^6 C). The CAT (corresponding to the temperature at the intersection between the lower horizontal portion of the plotted curve and the tangent line) was found to be 18 °C. These results thus showed that our HA derivative is able to self-assemble into nanogels at room temperature.

Dynamic light scattering measurements at 37 °C showed that the nanogels had a hydrodynamic diameter around 150 nm with a low polydispersity index (PDI) of 0.21 (Table 3).

In order to increase the colloidal stability of the resulting nanogels, they were crosslinked via hydrazone-bond formation between the ketone functions of the terpolymer and a bishydrazide, isophtalic dihydrazide (IDH), in aqueous medium (Fig. 1). The crosslinking step was carried out using an IDH to ketone molar ratio of 1 in order to ensure that all nanogels were sufficiently crosslinked to be stable at low temperature (Garcia et al., 2018). After purification of the crosslinked nanogels by dialysis, freeze-drying and redispersion of the sample in PBS (pH 7.4), the DLS analyses demonstrated the presence of nanogels below the CAT (Fig. 6C). The nanogels at 37 °C have a diameter below 150 nm while at 5 °C, their diameter is ~250 nm (Table 3 and Fig. 6C). The larger size of the nanogels at 5 °C can be attributed to increased hydration of the crosslinked copolymer chains, resulting in the nanogel swelling. TEM imaging indicated the presence of spherical particles, with sizes ranging from 50 to 120 nm (Fig. 6D). The size of the nanogels appeared to be smaller due to shrinkage during drying.

3.2.3. *Stability of nanogels after freeze-drying*

Freeze-drying is an attractive method for long-term storage of nanocarriers. In order to assess the stability of the nanogels over time after freeze-drying, the crosslinked nanogels were freeze-dried and then, stored in the freezer at −20 °C in a solid form. The study was carried out for ten weeks with a measurement once a week. After obtaining the dry powders, the nanogel suspensions were reconstituted in PBS according to the original volume at a concentration of 0.5 g/L. The aliquot was 0.8 µm pore size syringe filtered and then, analyzed by DLS at 5 and 37 °C. The results are shown in Fig. 7.

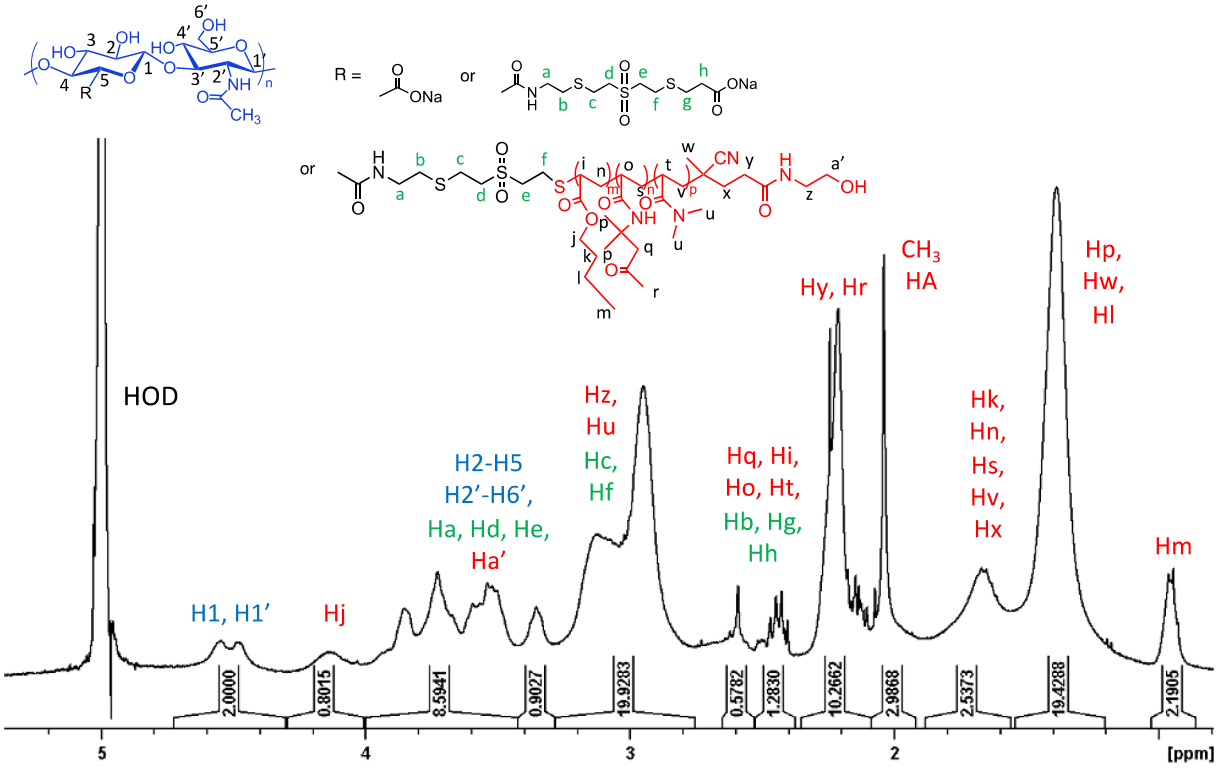

Fig. 5. ^{1}H NMR spectrum of HA-VS-poly(DAAM-*co*-DMA-co-BA) (400 MHz, 5 °C, 6 mg/mL in D_2O).

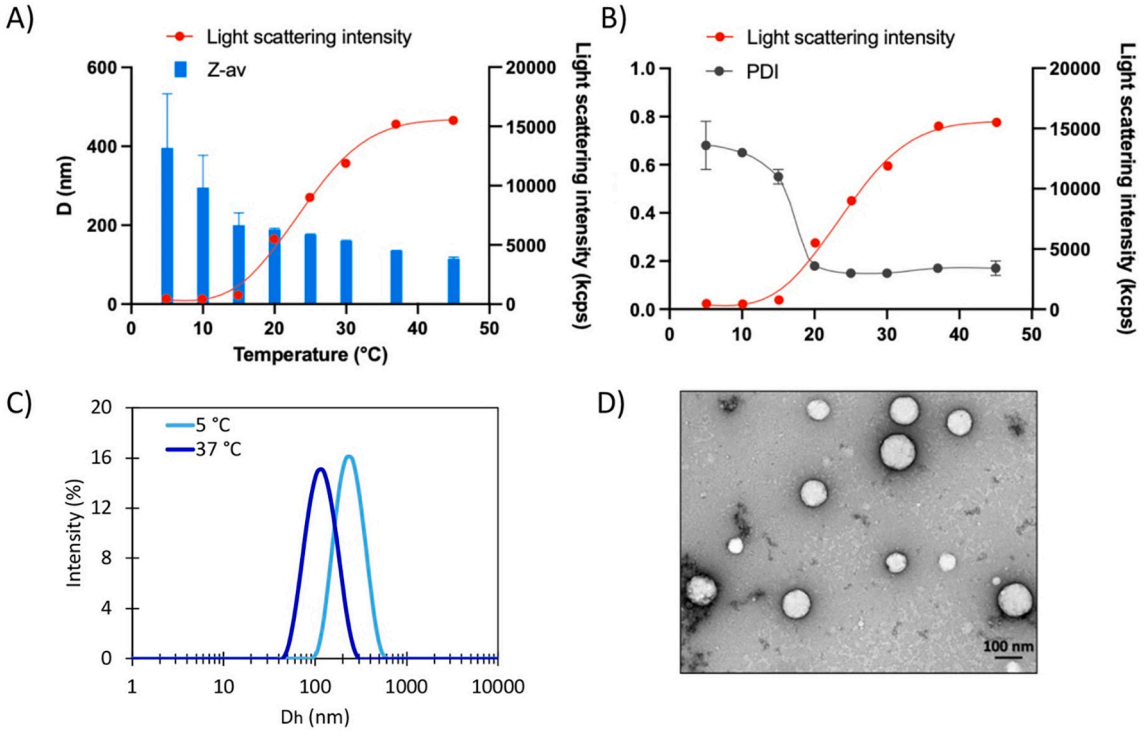

Fig. 6. A) and B) Analysis by DLS of the temperature sensitivity of HA-VS-poly(DAAM-co-DMA-co-BA) at 0.5 g/L in PBS (pH 7.4). C) Temperature responsiveness of crosslinked nanogels based on HA-VS-poly(DAAM-co-DMA-co-BA) analyzed by DLS. D) TEM image of the crosslinked nanogels at room temperature (0.5 g/L in PBS).

Table 3
Average diameter and PDI of HA-p-poly(DAAM-co-DMA) nanogels.

	5 °C		37 °C	
	Diameter[a] (nm)	PDI	Diameter (nm)[a]	PDI
Non-crosslinked nanogels	–[b]	–[b]	149 ± 3	0.21 ± 0.01
Crosslinked nanogels	249 ± 5	0.15 ± 0.02	122 ± 2	0.15 ± 0.01

[a] *Z*-Average diameter.
[b] No nanogel formation below the CAT.

The data shown in Fig. 7A are consistent with those presented in the previous section. Indeed, the diameter of the nanogels is in the range 110–130 nm at 37 °C, and in the range 220–250 nm at 5 °C throughout the study. The PDI values are rather stable at 37 °C (PDI ~ 0.16–0.19) during the ten weeks. At 5 °C, the variation of the PDI is slightly greater, ranging from 0.15 to 0.2. These results thus demonstrated the good stability of nanogels upon storage after freeze-drying.

The ability to store the nanogels as dry powders without modification of their size may offer the opportunity to vary the concentration of the nanogels formulation after aqueous redispersion. In order to verify this, the HA-based nanocarriers were dispersed in PBS at pH 7.4 at increasing concentrations from 0.5 to 3 g/L, 0.8 µm pore size syringe filtered and then, analyzed by DLS at 5 and 37 °C. The results are presented in Fig. 7B.

The DLS data show that at 5 and 37 °C, the nanogel diameter and the PDI vary slightly with increasing concentration. Interestingly, the measurement of the LSI at different concentrations of nanogels revealed that the LSI varies linearly with the nanogels concentration (Fig. S13). The proportionality relationship expected in this case (LSI $\propto D^6$ C) is therefore well validated and confirms that it is possible to obtain nanogels in solution up to 3 g/L without formation of aggregates and without sedimentation phenomenon.

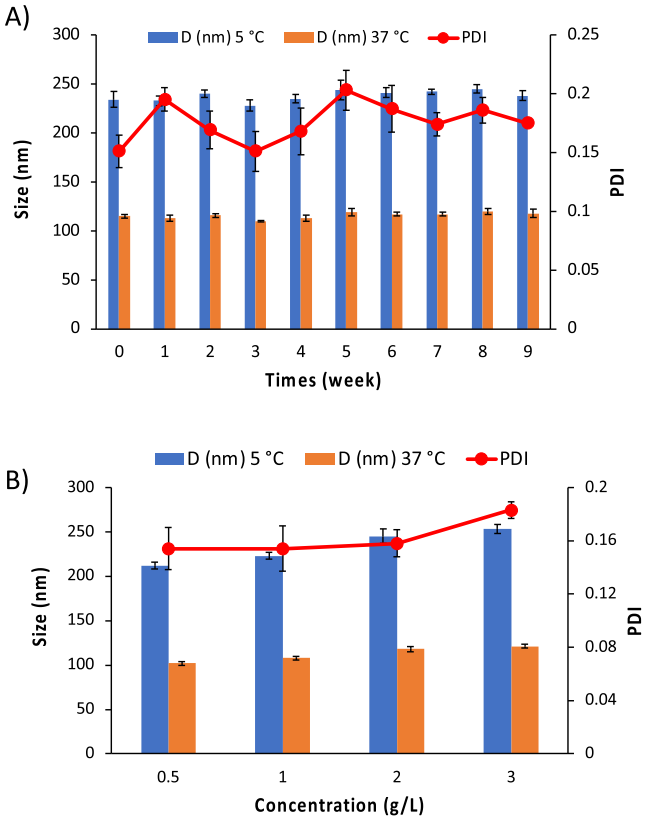

Fig. 7. A) Analysis by DLS of the stability upon storage in dry state of the crosslinked nanogels based on HA-VS-poly(DAAM-*co*-DMA-co-BA) redispersed at 0.5 g/L in PBS, pH = 7.4. B) Analysis of the effect of nanogels concentration on their size and polydispersity.

3.2.4. Encapsulation of aza-BODIPY-BSH in the HA-based nanogels

The HA-VS-poly(DAAM-co-DMA-co-BA) nanogels were loaded with aza-BODIPY-BSH by simply adding a concentrated organic solution of the ^{10}B-rich fluorochrome to the nanogels suspension, at 37 °C. After two hours, non-entrapped molecules were removed by filtration (0.8 µm pore size membrane). Then, the aza-BODIPY-BSH-loading ("drug-loading", DL) of the sample was measured by HPLC using the method described in the experimental section.

Several encapsulation assays were carried out by varying the concentration of the fluorochrome aza-BODIPY-BSH from 40 to 1100 µg/mL as well as that of the nanogels (0.5 and 3 g/L) to evaluate the maximum DL and encapsulation efficiency (EE).

The data shown in Fig. 8A indicated that the main objective, which was to obtain a final ^{10}B concentration of at least 40 µg/mL, was achieved with HA based nanogels dispersed at a concentration of 3 g/L. Indeed, a concentration of 537 µg/mL of encapsulated aza-BODIPY-BSH (corresponding to 45 µg/mL of ^{10}B) is achieved, when the fluorochrome is added at an initial concentration of 1100 µg/mL to the nanogel. These encapsulation conditions led to the highest DL obtained (18%, see Table S2). The ^{10}B concentration was calculated taking into account the fact that this fluorochrome contains a ^{10}B-enriched BSH (12 atoms) as well as an unenriched boron atom in the center of the molecule (the natural abundance of ^{10}B is ~20%). As compared to BPA which mass percentage of boron reaches 4.8%, the nanoformulation contained 1.5% of boron. However, each HA based nanogel gathers several aza-BODIPY-BSH molecules, which can allow the cell internalization of a large amount of boron per nanogel.

Regarding the encapsulation efficiency, the values derived from all these assays ranged from 49 to 67% (Table S2).

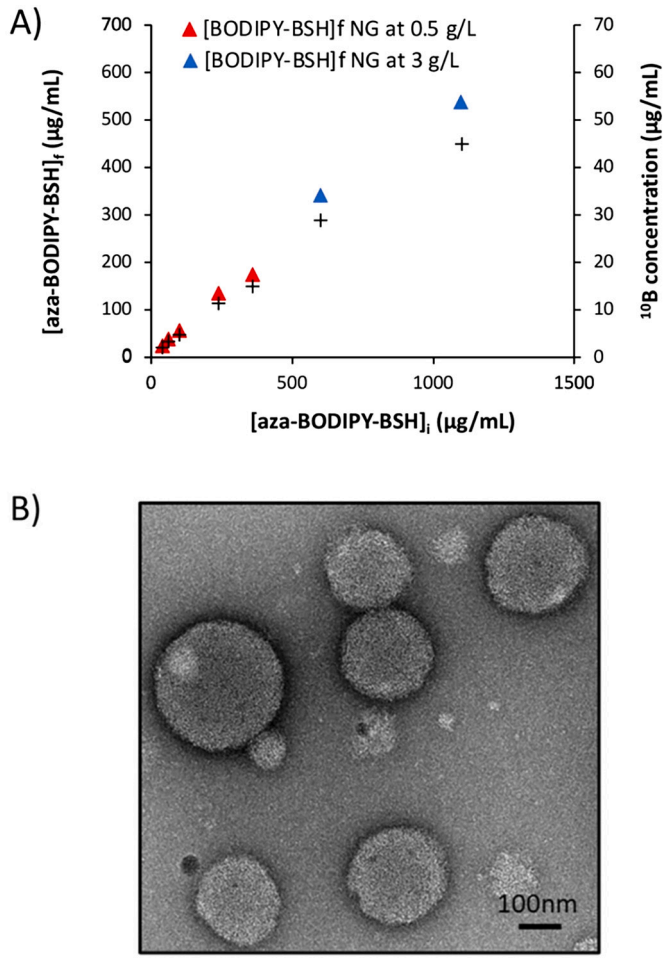

Fig. 8. A) Concentration of aza-BODIPY-BSH encapsulated in the nanogels (NG) as a function of the initial concentration of the fluorochrome added to the nanogels. B) TEM image of the crosslinked nanogels at 0.5 g/L in PBS containing aza-BODIPY-BSH ([aza-BODIPY-BSH] = 537 µg/mL).

4. In vitro cellular toxicity and uptake evaluation of nanogels based on HA-VS-(DAAM-co-DMA-co-BA)

The nanogels were evaluated for biological assays. First, cell toxicity was assessed on human endothelial cells HDMEC (Fig. 9A) and glioblastoma U87-MG (Fig. S12) to evidence the impact of the nanogel formulation (HA NG) as compared to the linear HA itself for 24 h, in the absence of BSH. Cell viability was not significantly affected by the compounds in our conditions, and similar results were observed for the two cell types.

Then, to evidence cell uptake and behavior, different samples of nanogels loaded with aza-BODIPY-BSH (Table 4) were incubated with U87-MG cells cultured in 2D at 50 µg/mL, and observed 24 h after incubation using confocal imaging (Fig. 9 B-E).

The near-infrared fluorescent signal of the aza-BODIPY-BSH and Cy7 contained within the nanogels was recorded in addition to the nuclear blue staining of Hoechst. While no fluorescence was detected in the control condition (Fig. 9B), the different formulations revealed the presence of the nanogels inside the cells, 24 h after incubation. The fluorescence was localized inside small vesicles contained in the cell cytoplasm. As indicated in Fig. 9D, the fluorescence was limited, when the cells were incubated with the nanoformulation **1** highly concentrated in aza-BODIPY-BSH. Such phenomenon might be due to the self-quenching of the dye that may occur at high local concentration (see Fig. S5). In the presence of Cy7 (HA NG **2**), the fluorescent signal was increased, and presented similar cell distribution, with vesicles close to the nucleus (Fig. 9C). Finally, at low aza-BODIPY-BSH concentration (HA NG **3**), the red fluorescent signal was restored, and evidenced a huge accumulation of the nanoformulation inside the cells (Fig. 9E).

5. In vivo biodistribution of nanogels

Theranostic compounds for BNCT application should be able to distribute in the body, to accumulate in the tumor, and to be eliminated without any undesired accumulation. To evaluate the behavior of the

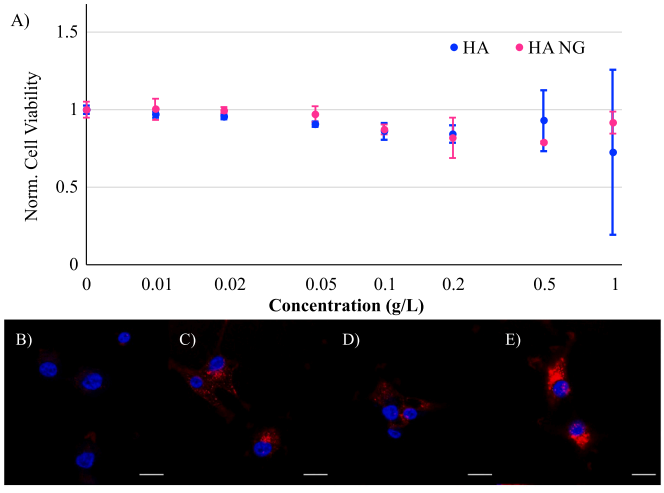

Fig. 9. A) In vitro cell viability of HDMEC normal endothelial cells following incubation with HA and HA NG. B) Glioblastoma U87-MG control cells, and behavior of the nanoformulations on U87-MG cells incubated for 24 h with 50 µg/mL of **2**C), **1** D), and **3** E) (red signal). Cell nuclei were stained with Hoechst 33342 (Blue signal). Scale bar: 20 µm. (For interpretation of the references to colour in this figure legend, the reader is referred to the web version of this article.)

Table 4
HA-based nanogels selected for biological evaluations.[b]

HA NG	Cy7 labeling	[HA NG] (g/L)	$[aza\text{-}BODIPY]_f$ (μg/mL)
1	No	3	562 ± 39
2	Yes	3	625 ± 44
3	No	1	136 ± 10

[b] % in mass of nanogels.

nanoformulation, the HA based nanogel **1** containing high aza-BODIPY-BSH concentration was injected intravenously to mice-bearing subcutaneous U87-MG tumors, at 3 mg/mL. Mice were imaged from 2 to 48 h post injection, and organs were sampled to measure the fluorescence signal in the different organs at 24 and 48 h. As indicated in the Fig. 10A-B, the nanogels circulated in the animal's body, and were mainly eliminated by the liver and the spleen, as expected due to their size (> 100 nm) (Dufort et al., 2012; Longmire et al., 2011). The subcutaneous tumors accumulated a part of the nanogels, with a Tumor-to-Muscle ratios around 6, both at 24 and 48 h, and Tumor-to-normal Brain around 2 (Fig. 10C). As reported for in vitro investigations, high local concentration of nanogel may induce a self-quenching of the fluorescence, which could underestimate the tumor accumulation; an ICP-AES quantification of the boron amount could be helpful to confirm such results. However, for BNCT applications, ideal ratios between tumor lesions and surrounding tissues should be >2.5. In clinics, the amount of BSH accumulated in the tumor is estimated from blood sampling. This is an imperfect procedure, due to the heterogeneity among patients and lesions, that still occurs (Wittig et al., 2011). Using intravenous administration of BSH, very weak amount of boron was measured in normal brain of patients (Hideghety et al., 2003), while local administration (as convection-enhanced delivery for brain tumors) may increase tumor accumulation and retention (Futamura et al., 2017). Most of the Tumor-to-Brain ratios measured from preclinical experiments and clinical trials were around 1 or below (Wittig et al., 2011). Therefore, the ratios obtained in this work are favorable for BNCT applications for brain lesions. A strategy to improve tumor accumulation may consist in reducing hepatic uptake by optimizing the size of HA-based nanoformulation and/or by modifying the chemical composition of the hydrophilic shell. The addition of a poly(ethylene glycol) (PEG) to nanoparticles possessing a hydrophilic shell based on HA have been recently reported to combine the advantages of active targeting via HA-CD44 recognition and reduction of RES phagocytosis to synergistically facilitate the tumor accumulation of the nanoformulation (Luo et al., 2020).

Finally, the nanogel's behavior was evaluated on fertilized chicken eggs, with U87-MG tumor cells implanted on the chorioallantoic membrane (CAM). The pharmacokinetic of tumor uptake was monitored using optical imaging and evidenced an increase of tumor accumulation during the first hours after administration, a plateau between 2.5 and 5 h post injection, and a decrease after 5 h (Fig. 10 D-E). Between 2.5 and 5 h, the tumor accumulation was almost stable (15.5 ± 4.8 vs. 14.8 ± 6.7, respectively). This CAM assay indicated a stable and prolonged ^{10}B accumulation at the tumor site between 2.5 and 5 h post-injection, a criterion that is mandatory for BNCT applications (Sauerwein et al., 2021).

6. Conclusions

We prepared a thermosensitive terpolymer poly(DAAM-*co*-DMA-co-BA) with a T_{cp} around 10 °C and coupled it to HA via thiol-vinylsulfone. The HA derivative was able to self-assemble into nanogels at room temperature, with a hydrodynamic diameter around 150 nm. The colloidal stability was ensured through crosslinking via hydrazone-bond formation allowing the freeze-drying of the nanogels for long-term stability, and re-dispersion at high concentration. In the perspective of theranostic BNCT application, aza-BODIPY-BSH was efficiently encapsulated within the nanogels, reaching 45 μg/mL of ^{10}B. While the nanoformulation was not toxic on normal endothelial cells, it accumulated efficiently in U87-MG glioblastoma cells in vitro, into small cytoplasmic vesicles. After intravenous administration, the aza-BODIPY-BSH-rich nanogel distributed in the body, indicating a hepatobiliary elimination route. The accumulation in the tumor was prolonged and stable during >2 h. The different measured ratios indicated a Tumor/Normal brain higher than BSH alone (≤ 1 (Wittig et al., 2011)) and reaching almost 6 versus muscle. Such results indicated that the nanogel formulation may be of interest for BNCT application for brain lesions and probably for sarcoma. Additionally, aza-BODIPYs being very versatile might be linked to specific chelate as DOTA derivatives for quantitative nuclear imaging in perspective of clinical application (Lhenry et al., 2015).

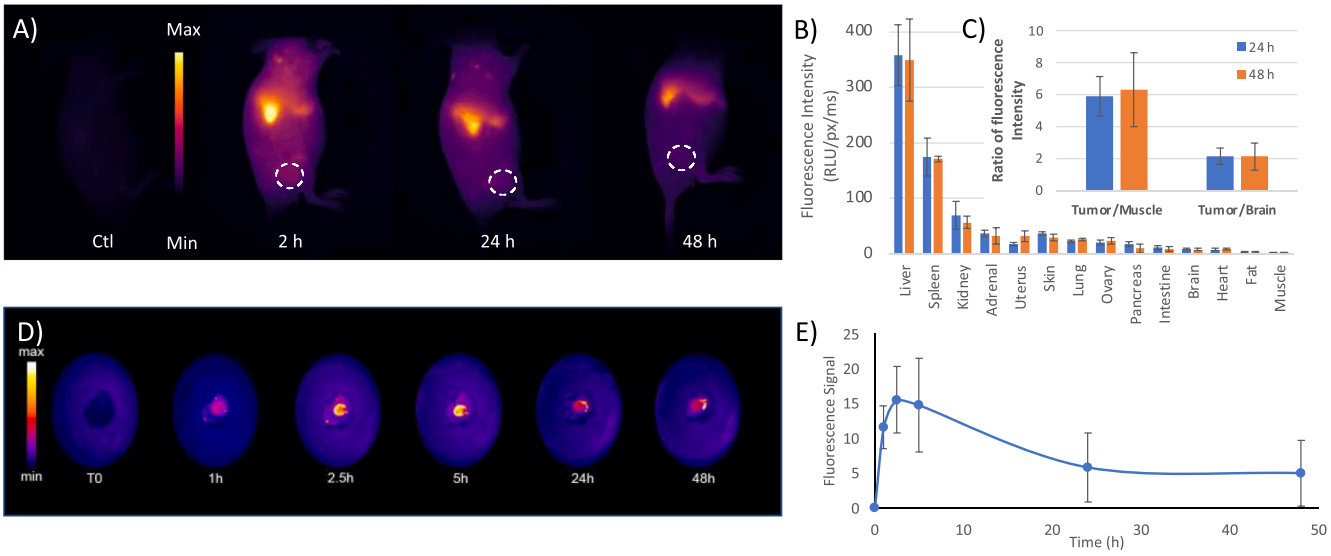

Fig. 10. In vivo behavior of HA nanogel. A) Representative fluorescence images of mice-bearing subcutaneous U87-MG tumor (white circle), before, and at 2, 24 and 48 h after administration of HA nanogels loaded with aza-BODIPY-^{10}B-BSH. B) and C) Fluorescence intensities of the remoted organs from A) (n = 3). D) 2D-Fluorescence imaging of HA nanogels loaded with aza-BODIPY-^{10}B-BSH distribution before and until 48 h post-administration onto U87-MG tumors implanted on the chorioallantoic membrane (CAM) of fertilized chicken egg. E) Non-invasive measurement of HA nanogels loaded with aza-BODIPY-^{10}B-BSH fluorescence in tumors (from D) with time. Results are expressed as the tumor fluorescence mean ± S·D (n = 4).

CRediT authorship contribution statement

Simon Coninx: Investigation, Writing – original draft. **Ghadir Kalot:** Investigation. **Amélie Godard:** Investigation, Writing – review & editing. **Ewen Bodio:** Investigation, Writing – review & editing. **Christine Goze:** Investigation, Writing – review & editing. **Lucie Sancey:** Conceptualization, Validation, Writing – review & editing, Supervision. **Rachel Auzély-Velty:** Conceptualization, Validation, Writing – review & editing, Supervision.

Declaration of Competing Interest

The authors declare that they have no known competing financial interests or personal relationships that could have appeared to influence the work reported in this paper.

Data availability

No data was used for the research described in the article.

Acknowledgments

The authors are grateful to Dr. X. Le Guével and Dr. V. Josserand from OPTIMAL, small animal imaging platform (Grenoble, www.optimal-plateforme.fr) for technical development and access to optical devices. The authors also thank J.-L. Puteaux and C. Lancelon-Pin for the TEM observations at the microscopy platform of ICMG (FR2607); I. Jeacomine at the NMR platform of ICMG for her support; S. Ortega for her support in HPLC analyses; V. Cosenza for her support in chemical syntheses; I. Otsuka for SEC analyses; F. Dalonneau for cell toxicity. The authors also would like to acknowledge the different financial supports: La Ligue Contre le Cancer (Doctoral training grant to SC); Oncostarter project of the cancérôpole CLARA (AGNOSTIC project); the "Agence Nationale pour la Recherche" in the framework of the Nanovax project (ANR-16-ENM2-0007-03); GEFLUC Grenoble Dauphiné Savoie; FLI (France Life Imaging) for the project Thera-BODIPY; the CNRS Mission for Transversal and Interdisciplinary Initiatives for the project BREVET-ISOTOP, the Fondation pour la Recherche Médicale (FRM) for the specific support of G.K. (FRM ECO201806006861). This research was funded by The Ministère de l'Enseignement Supérieur et de la Recherche, the Centre National de la Recherche Scientifique (CNRS), the Conseil Régional de Bourgogne (PhD JCE Grant # 2015-9205AAO033S04139/BG0003203), and the French Research National Agency (ANR) via project JCJC "WazaBY" ANR-18-CE18-0012. This work is part of the projects "Pharmacoimagerie et agents théranostiques" et "Chimie durable, environnement et agroalimentaire" supported by the Université de Bourgogne and the Conseil Régional de Bourgogne through the Plan d'Actions Régional pour l'Innovation (PARI) and the European Union through the PO FEDER-FSE Bourgogne 2014/2020 programs. It was performed within the Dijon's pharmaco-imaging consortium, a regional center of excellence in pharmaco-imaging.

Appendix A. Supplementary data

Supplementary data to this article can be found online at https://doi.org/10.1016/j.ijpx.2022.100134.

References

Auzenne, E., Ghosh, S.C., Khodadadian, M., Rivera, B., Farquhar, D., Price, R.E., Ravoori, M., Kundra, V., Freedman, R.S., Klostergaard, J., 2007. Hyaluronic acid-paclitaxel: antitumor efficacy against CD44(+) human ovarian carcinoma xenografts. Neoplasia (Ann Arbor, MI, United States) 9, 479–486.

Bertrand, B., Passador, K., Goze, C., Denat, F., Bodio, E., Salmain, M., 2018. Metal-based BODIPY derivatives as multimodal tools for life sciences. Coord. Chem. Rev. 358, 108–124.

Choi, K.Y., Saravanakumar, G., Park, J.H., Park, K., 2012. Hyaluronic acid-based nanocarriers for intracellular targeting: interfacial interactions with proteins in cancer. Colloids Surf., B 99, 82–94.

Di Meo, C., Panza, L., Capitani, D., Mannina, L., Banzato, A., Rondina, M., Renier, D., Rosato, A., Crescenzi, V., 2007. Hyaluronan as carrier of carboranes for tumor targeting in Boron neutron capture therapy. Biomacromolecules 8, 552–559.

Draffin, J.E., McFarlane, S., Hill, A., Johnston, P.G., Waugh, D.J.J., 2004. CD44 potentiates the adherence of metastatic prostate and breast cancer cells to bone marrow endothelial cells. Cancer Res. 64, 5702–5711.

Dufort, S., Sancey, L., Coll, J.L., 2012. Physico-chemical parameters that govern nanoparticles fate also dictate rules for their molecular evolution. Adv. Drug Deliv. Rev. 64, 179–189.

Dymova, M.A., Taskaev, S.Y., Richter, V.A., Kuligina, E.V., 2020. Boron neutron capture therapy: current status and future perspectives. Cancer Commun (Lond) 40, 406–421.

Feiner, I.V.J., Pulagam, K.R., Uribe, K.B., Passannante, R., Simo, C., Zamacola, K., Gomez-Vallejo, V., Herrero-Alvarez, N., Cossio, U., Baz, Z., Caffarel, M.M., Lawrie, C. H., Vugts, D.J., Rejc, L., Llop, J., 2021. Pre-targeting with ultra-small nanoparticles: boron carbon dots as drug candidates for boron neutron capture therapy. J. Mater. Chem. B 9, 410–420.

Futamura, G., Kawabata, S., Nonoguchi, N., Hiramatsu, R., Toho, T., Tanaka, H., Masunaga, S.I., Hattori, Y., Kirihata, M., Ono, K., Kuroiwa, T., Miyatake, S.I., 2017. Evaluation of a novel sodium borocaptate-containing unnatural amino acid as a boron delivery agent for neutron capture therapy of the F98 rat glioma. Radiat. Oncol. 12, 26.

Garcia, F.P., Rippe, M., Companhoni, M.V.P., Stefanello, T.F., Louage, B., Van Herck, S., Sancey, L., Coll, J.L., De Geest, B.G., Vataru Nakamura, C., Auzely-Velty, R., 2018. A versatile method for the selective core-crosslinking of hyaluronic acid nanogels via ketone-hydrazide chemistry: from chemical characterization to in vivo biodistribution. Biomater. Sci. 6, 1754–1763.

Gonzalez-Campo, A., Ferrer-Ugalde, A., Vinas, C., Teixidor, F., Sillanpaa, R., Rodriguez-Romero, J., Santillan, R., Farfan, N., Nunez, R., 2013. A versatile methodology for the controlled synthesis of photoluminescent high-boron-content dendrimers. Chemistry 19, 6299–6312.

Grover, G.N., Alconcel, S.N.S., Matsumoto, N.M., Maynard, H.D., 2009. Trapping of thiol-terminated acrylate polymers with divinyl sulfone to generate well-defined semitelechelic Michael acceptor polymers. Macromol. (Washington, DC, U. S.) 42, 7657–7663.

Hideghety, K., Sauerwein, W., Wittig, A., Gotz, C., Paquis, P., Grochulla, F., Haselsberger, K., Wolbers, J., Moss, R., Huiskamp, R., Fankhauser, H., de Vries, M., Gabel, D., 2003. Tissue uptake of BSH in patients with glioblastoma in the EORTC 11961 phase I BNCT trial. J. Neuro-Oncol. 62, 145–156.

Ho, S.L., Yue, H., Tegafaw, T., Ahmad, M.Y., Liu, S., Nam, S.W., Chang, Y., Lee, G.H., 2022. Gadolinium neutron capture therapy (GdNCT) agents from molecular to nano: current status and perspectives. ACS Omega. 7, 2533–2553.

Huang, L.-C.S., Le, D., Hsiao, I.L., Fritsch-Decker, S., Hald, C., Huang, S.-C., Chen, J.-K., Hwu, J.R., Weiss, C., Hsu, M.-H., Delaittre, G., 2021. Boron-rich, cytocompatible block copolymer nanoparticles by polymerization-induced self-assembly. Polym. Chem. 12, 50–56.

Kalot, G., Godard, A., Busser, B., Pliquett, J., Broekgaarden, M., Motto-Ros, V., Wegner, K.D., Resch-Genger, U., Koster, U., Denat, F., Coll, J.L., Bodio, E., Goze, C., Sancey, L., 2020. Aza-BODIPY: a new vector for enhanced theranostic boron neutron capture therapy applications. Cells 9, 1953.

Kikuchi, S., Kanoh, D., Sato, S., Sakurai, Y., Suzuki, M., Nakamura, H., 2016. Maleimide-functionalized closo-dodecaborate albumin conjugates (MID-AC): unique ligation at cysteine and lysine residues enables efficient boron delivery to tumor for neutron capture therapy. J. Control. Release 237, 160–167.

Kono, Y., Kurihara, H., Kawamoto, H., Yasui, N., Honda, N., Igaki, H., Itami, J., 2017. Radiation absorbed dose estimates for 18F-BPA PET. Acta Radiol. 58, 1094–1100.

Le Guevel, X., Henry, M., Motto-Ros, V., Longo, E., Montanez, M.I., Pelascini, F., de La Rochefoucauld, O., Zeitoun, P., Coll, J.L., Josserand, V., Sancey, L., 2018. Elemental and optical imaging evaluation of zwitterionic gold nanoclusters in glioblastoma mouse models. Nanoscale 10, 18657–18664.

Lhenry, D., Larrouy, M., Bernhard, C., Goncalves, V., Raguin, O., Provent, P., Moreau, M., Collin, B., Oudot, A., Vrigneaud, J.M., Brunotte, F., Goze, C., Denat, F., 2015. BODIPY: a highly versatile platform for the design of bimodal imaging probes. Chemistry 21, 13091–13099.

Li, J., Shi, Y., Zhang, Z., Liu, H., Lang, L., Liu, T., Chen, X., Liu, Z., 2019. A metabolically stable boron-derived tyrosine serves as a theranostic agent for positron emission tomography guided boron neutron capture therapy. Bioconjug. Chem. 30, 2870–2878.

Li, J., Sun, Q., Lu, C., Xiao, H., Guo, Z., Duan, D., Zhang, Z., Liu, T., Liu, Z., 2022. Boron encapsulated in a liposome can be used for combinational neutron capture therapy. Nat. Commun. 13, 2143.

Longmire, M.R., Ogawa, M., Choyke, P.L., Kobayashi, H., 2011. Biologically optimized nanosized molecules and particles: more than just size. Bioconjug. Chem. 22, 993–1000.

Luo, Y., Prestwich, G.D., 1999. Synthesis and selective cytotoxicity of a hyaluronic acid-antitumor bioconjugate. Bioconjug. Chem. 10, 755–763.

Luo, K., Yin, S., Zhang, R., Yu, H., Wang, G., Li, J., 2020. Multifunctional composite nanoparticles based on hyaluronic acid-paclitaxel conjugates for enhanced cancer therapy. Int. J. Pharm. (Amsterdam, Neth.) 589, 119870.

Malouff, T.D., Seneviratne, D.S., Ebner, D.K., Stross, W.C., Waddle, M.R., Trifiletti, D.M., Krishnan, S., 2021. Boron neutron capture therapy: a review of clinical applications. Front. Oncol. 11, 601820.

Michiue, H., Sakurai, Y., Kondo, N., Kitamatsu, M., Bin, F., Nakajima, K., Hirota, Y., Kawabata, S., Nishiki, T., Ohmori, I., Tomizawa, K., Miyatake, S., Ono, K., Matsui, H., 2014. The acceleration of boron neutron capture therapy using multi-linked mercaptoundecahydrododecaborate (BSH) fused cell-penetrating peptide. Biomaterials 35, 3396–3405.

Musnier, B., Wegner, K.D., Comby-Zerbino, C., Trouillet, V., Jourdan, M., Hausler, I., Antoine, R., Coll, J.L., Resch-Genger, U., Le Guevel, X., 2019. High photoluminescence of shortwave infrared-emitting anisotropic surface charged gold nanoclusters. Nanoscale 11, 12092–12096.

Nakase, I., Katayama, M., Hattori, Y., Ishimura, M., Inaura, S., Fujiwara, D., Takatani-Nakase, T., Fujii, I., Futaki, S., Kirihata, M., 2019. Intracellular target delivery of cell-penetrating peptide-conjugated dodecaborate for boron neutron capture therapy (BNCT). Chem. Commun. (Camb.) 55, 13955–13958.

Nomoto, T., Yao, Y., Inoue, Y., Suzuki, M., Kanamori, K., Takemoto, H., Matsui, M., Tomoda, K., Nishiyama, N., 2021. Fructose-functionalized polymers to enhance therapeutic potential of p-boronophenylalanine for neutron capture therapy. J. Control. Release 332, 184–193.

Pitto-Barry, A., 2021. Polymers and boron neutron capture therapy (BNCT): a potent combination. Polym. Chem. 12, 2035–2044.

Pulagam, K.R., Gona, K.B., Gomez-Vallejo, V., Meijer, J., Zilberfain, C., Estrela-Lopis, I., Baz, Z., Cossio, U., Llop, J., 2019. Gold nanoparticles as boron carriers for boron neutron capture therapy: synthesis, radiolabelling and in vivo evaluation. Molecules 24, 3609.

Qhattal, H.S.S., Liu, X., 2011. Characterization of CD44-mediated cancer cell uptake and intracellular distribution of hyaluronan-grafted liposomes. Mol. Pharm. 8, 1233–1246.

Rippe, M., Cosenza, V., Auzely-Velty, R., 2019a. Design of soft nanocarriers combining hyaluronic acid with another functional polymer for cancer therapy and other biomedical applications. Pharmaceutics 11, 338.

Rippe, M., Stefanello, T.F., Kaplum, V., Britta, E.A., Garcia, F.P., Poirot, R., Companhoni, M.V.P., Nakamura, C.V., Szarpak-Jankowska, A., Auzely-Velty, R., 2019b. Heparosan as a potential alternative to hyaluronic acid for the design of biopolymer-based nanovectors for anticancer therapy. Biomater. Sci. 7, 2850–2860.

Ruan, Z., Liu, L., Fu, L., Xing, T., Yan, L., 2016. An amphiphilic block copolymer conjugated with carborane and a NIR fluorescent probe for potential imaging-guided BNCT therapy. Polym. Chem. 7, 4411–4418.

Sauerwein, W., Wittig, A., Moss, R., Nakagawa, Y., 2012. Drugs for BNCT: BSH and BPA. In: Neutron Capture Therapy. Principles and Application. Springer, Berlin/Heidelberg, Germany, pp. 117–160.

Sauerwein, W.A.G., Sancey, L., Hey-Hawkins, E., Kellert, M., Panza, L., Imperio, D., Balcerzyk, M., Rizzo, G., Scalco, E., Herrmann, K., Mauri, P., De Palma, A., Wittig, A., 2021. Theranostics in boron neutron capture therapy. Life (Basel) 11, 330.

Shi, Y., Li, J., Zhang, Z., Duan, D., Zhang, Z., Liu, H., Liu, T., Liu, Z., 2018. Tracing boron with fluorescence and positron emission tomography imaging of boronated porphyrin nanocomplex for imaging-guided boron neutron capture therapy. ACS Appl. Mater. Interfaces 10, 43387–43395.

Shirakawa, M., Zaboronok, A., Nakai, K., Sato, Y., Kayaki, S., Sakai, T., Tsurubuchi, T., Yoshida, F., Nishiyama, T., Suzuki, M., Tomida, H., Matsumura, A., 2021. A novel boron lipid to modify liposomal surfaces for boron neutron capture therapy. Cells 10, 3421.

Skwierawska, D., Lopez-Valverde, J.A., Balcerzyk, M., Leal, A., 2022. Clinical viability of boron neutron capture therapy for personalized radiation treatment. Cancers (Basel) 14, 2865.

Stewart, S.A., Coulson, M.B., Zhou, C., Burke, N.A.D., Stover, H.D.H., 2018. Synthetic hydrogels formed by thiol-ene crosslinking of vinyl sulfone-functional poly(methyl vinyl ether-alt-maleic acid) with α,ω-dithio-polyethylene glycol. Soft Matter 14, 8317–8324.

Sumitani, S., Nagasaki, Y., 2012. Boron neutron capture therapy assisted by boron-conjugated nanoparticles. Polym. J. (Tokyo, Japan) 44, 522–530.

Sumitani, S., Oishi, M., Yaguchi, T., Murotani, H., Horiguchi, Y., Suzuki, M., Ono, K., Yanagie, H., Nagasaki, Y., 2012. Pharmacokinetics of core-polymerized, boron-conjugated micelles designed for boron neutron capture therapy for cancer. Biomaterials 33, 3568–3577.

Wittig, A., Stecher-Rasmussen, F., Hilger, R.A., Rassow, J., Mauri, P., Sauerwein, W., 2011. Sodium mercaptoundecahydro-closo-dodecaborate (BSH), a boron carrier that merits more attention. Appl. Radiat. Isot. 69, 1760–1764.

Yoneoka, S., Park, K.C., Nakagawa, Y., Ebara, M., Tsukahara, T., 2018. Synthesis and evaluation of thermoresponsive boron-containing poly(N-isopropylacrylamide) diblock copolymers for self-assembling nanomicellar boron carriers. Polymers (Basel) 11, 42.

Zaboronok, A., Yamamoto, T., Nakai, K., Yoshida, F., Uspenskii, S., Selyanin, M., Zelenetskii, A., Matsumura, A., 2015. Hyaluronic acid as a potential boron carrier for BNCT: preliminary evaluation. Appl. Radiat. Isot. 106, 181–184.